Article ID: 1000-324X(2023)06-0701-07 **DOI:** 10.15541/jim20220478

Construction and Photocatalytic Activity of Monoclinic Tungsten Oxide/Red Phosphorus Step-scheme Heterojunction

TUERHONG Munire[1], ZHAO Honggang[1,2], MA Yuhua[1,2], QI Xianhui[1], LI Yuchen[1], YAN Chenxiang[1], LI Jiawen[1], CHEN Ping[1]

(1. College of Chemistry and Chemical Engineering, Xinjiang Normal University, Urumqi 830054, China; 2. Xinjiang Key Laboratory of Energy Storage and Photoelectrocatalytic Materials, Xinjiang Normal University, Urumqi 830054, China)

Abstract: S-scheme heterojunction has been extensively investigated for hydrogen evolution and environmental pollution issues. In this study, a monoclinic WO_3/hydrothermally treated red phosphorus (HRP) S-scheme composite was prepared by hydrothermal method. XPS and EPR characterization confirmed that the monoclinic WO_3/HRP composite formed S-scheme heterojunction. 5%WO_3/HRP composite displayed the optimal photocatalytic activity under visible light irradiation, and its degradation rate of Rhodamine B (RhB) reached 97.6% after 4 min of visible light irradiation, while its hydrogen evolution rate reached 870.69 μmol·h^{-1}·g^{-1} which was 3.62 times of that of pure HRP. This could be ascribed to the tight interfacial bonding between WO_3 and HRP, and the formation of S-scheme heterostructure, enabling rapid separation of photogenerated carriers and therefore improving the strong redox capacity. This study provided a promising RP-based photocatalyst to meet the demand for clean energy and drinking water.

Key words: WO_3; red phosphorus; photocatalytic hydrogen evolution; S-scheme heterojunction

Red phosphorous (RP) is one of the most abundant, inexpensive, less toxic, and easily available materials[1-3]. It possesses strong visible light absorption, and has great potential for photocatalytic applications[4]. However, the photogenerated electron and hole are easily recombined in photocatalytic efficiency, which greatly limits its application because of RP large particle size and agglomeration[5]. RP is combined with other semiconductor material to construct heterojunction, which can effectively overcome the above disadvantages and improve the photocatalytic activity[6], such as SnO_2/RP[7], Bi_2O_3/RP[8], $Bi_2O_2CO_3$/RP[9], g-C_3N_4/RP[10] and $Bi_2Fe_4O_9$/RP[11]. Therefore, it is necessary to find suitable semiconductor matching RP to build heterojunction.

Tungsten trioxide (WO_3), as a typical n-type semiconductor with narrow bandgap energy (2.4–2.8 eV)[12], was widely used in the management of environmental remediation[13]. Although remarkable advances have been made, the narrow band gap of WO_3 also causes fast recombination rate of photo-induced charges, leading to poor photocatalytic activity[14-15]. Compared with pure WO_3 and RP, WO_3/RP composite showed better hydrogen evolution, which could reduce the recombination of charge carriers[16]. However, WO_3/RP composites *via* a low temperature calcination method led to aggregation and decrease of the active sites of RP.

In this study, the WO_3/HRP S-scheme heterojunction was constructed through hydrothermal treatment. The photocatalytic performance was estimated by photocatalytic organic degradation and hydrogen evolution. Finally, the S-scheme heterojunction photocatalytic mechanism of WO_3/HRP composites was directly evidenced by *in situ* X-ray photoelectron spectroscopy (XPS) and electron paramagnetic resonance (EPR) results.

1 Experimental

1.1 Preparation of WO_3/HRP composite

Preparation of WO_3: $Na_2WO_4·2H_2O$ (60.63 mmol·L^{-1}) was dissolved in 50 mL of ultrapure water, then 0.9 mL

Received date: 2022-08-11; **Revised date:** 2022-10-17; **Published online:** 2022-11-16
Foundation item: National Natural Science Foundation of China (22208275, 52063028); College Students' Innovative Entrepreneurial Training (S202210762003, X202210762017, X202210762123); PhD Startup Fund of Xinjiang Normal University (XJNUBS1907); Innovation Team for Monitoring of Emerging Contaminants and Biomarkers (2021D14017)
Biography: TUERHONG Munire(1999–), female, Master candidate. E-mail: 1803882596@qq.com
吐尔洪·木尼热(1999–), 女, 硕士研究生. E-mail: 1803882596@qq.com
Corresponding author: ZHAO Honggang, lecturer. E-mail: 262385441@qq.com; MA Yuhua, associate professor. E-mail: 15199141253@163.com
赵红刚, 讲师. E-mail: 262385441@qq.com; 马玉花, 副教授. E-mail: 15199141253@163.com

of lactic acid was dropped into the solution and stirred for 15 min. Subsequently, pH of solution was adjusted to 1.0 using 6.0 mol·L^{-1} HCl. The solution was stirred for 30 min, and heated at 120 ℃ for 12 h, centrifuged. The obtained samples were washed with deionized water, dried at 60 ℃ for 5 h, and then calcined at 500 ℃ for 2 h.

Preparation of WO_3/HRP composites: HRP was treated according to Ref.[17]. The composite with HRP was obtained based on WO_3 mass fraction (3%, 5% and 7%), and the solution was hydrothermally treated at 150 ℃ for 4 h, centrifuged and washed for several times, and freeze-dried for 18 h to obtain WO_3/HRP composite and marked as 3%WO_3/HRP, 5%WO_3/HRP, and 7%WO_3/HRP, respectively.

1.2 Photocatalytic pollutant degradation

A 300 W Xe lamp (UV light was cutoff-filtered, 140 mW/cm^2) was used, and RhB was used as target pollutant. 5 mg photocatalyst was added into 20 mL RhB solution (10 mg·L^{-1}), and then stirred in dark for 30 min to ensure absorption-desorption equilibrium. During the irradiation process, the suspension was removed every 1 min for centrifugation and the absorbance of the residual RhB solution was determined by UV-Vis spectrophotometer at the maximum absorption wavelength (λ_{max}=554 nm).

1.3 Photocatalytic hydrogen evolution

Photocatalytic hydrogen production was carried out by using a 300 W Xe lamp (UV light was cutoff-filtered, 140 mW/cm^2). The generated hydrogen was *in situ* detected periodically using an online gas chromatography (GC-7900) with a thermal conductivity detector. 50 mg photocatalyst was dispersed in 80 mL solution containing Na_2SO_3 (0.35 mol·L^{-1}) and Na_2S (0.15 mol·L^{-1}) as the sacrifice agent, and the suspension was magnetically stirred under visible light irradiation.

2 Results and discussion

2.1 Photocatalyst characterization

The crystal structures of the HRP, WO_3 and 5%WO_3/HRP composite were analyzed by XRD patterns (Fig. 1). For pure HRP, the characteristic diffraction peak at 2θ=14.9° corresponded to (102) crystal plane, consistent with the reported results in the literature[17]. The characteristic peaks of WO_3 indexed at 2θ=22.8°, 24.1°, and 33.9° correspond to the planes (002), (020) and (200) facets (JCPDS 83-0951), according to the lattice parameters of monoclinic tungsten oxide[18-20]. For 5%WO_3/HRP composite, the diffraction peaks of the HRP and WO_3 were obviously present.

The surface chemical compositions of all samples

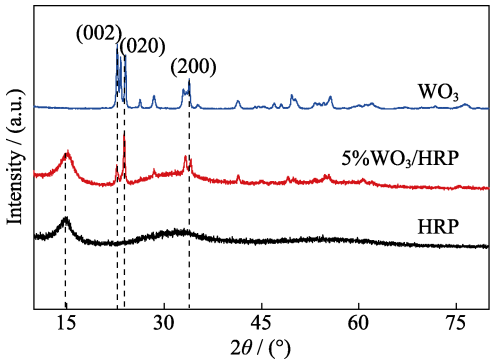

Fig. 1 XRD patterns of HRP, WO_3 and 5%WO_3/HRP composite

were characterized by FT-IR spectroscopy (Fig. S1). For pure HRP, the vibration absorption of the P–P–O, P–O and P=O bond located at 1008, 1178 and 1641 cm^{-1}, which was consistent with the characteristic absorption peaks of RP[21]. For pure WO_3, the absorption peaks at 956, 823 and 753 cm^{-1} were referred to W=O, O–W–O and W–O–W bonds[22]. The characteristic peaks of WO_3 and HRP functional groups were presented in the FT-IR spectrum of 5%WO_3/HRP, indicating the coexistence of WO_3 and HRP in the composite.

The morphologies of as-prepared samples were examined by SEM. HRP removed impurities from the surface of commercial RP, and its surface existed micropore (Fig. S2(a, d)). The typical morphology of WO_3 was rectangular nanoplates with a certain thickness (Fig. S2(b, e)). 5%WO_3/HRP composite revealed a large number of loose particles, which facilitates the improved light adsorption, and also provides abundant spaces for the anchoring of other particles (Fig. S2(c, f)). Furthermore, the basic elements of W, O, and P were present in the WO_3/HRP composite (Fig. S2(g, h). Thus, HRP and WO_3 coexisted in the WO_3/HRP composites.

The crystal structure and lattice orientation of each sample were further investigated through TEM. HRP surface was amorphous, and tiny folded, which was favorable to its surface adsorption properties (Fig. 2(a, b)). The WO_3 nanostructure exhibited regular sheet-like morphology structure, which was consistent with the SEM results (Fig. S2(c)). The lattice size was 0.37 nm that matched the distance (020) planes of monoclinic WO_3 structure, according to the lattice parameters of monoclinic WO_3 (JCPDS 83-0951)[18]. TEM images of 5%WO_3/HRP showed that there was an additional layer of homogeneous WO_3 on the surface of HRP and closely connected to each other, avoiding aggregation of HRP and forming a heterogeneous structure that facilitates interfacial charge transfer (Fig. 2(e, f)).

XPS survey spectra were conducted to investigate the chemical compositions and bonding configurations of the samples[23]. C, O, P and W were present in the composite

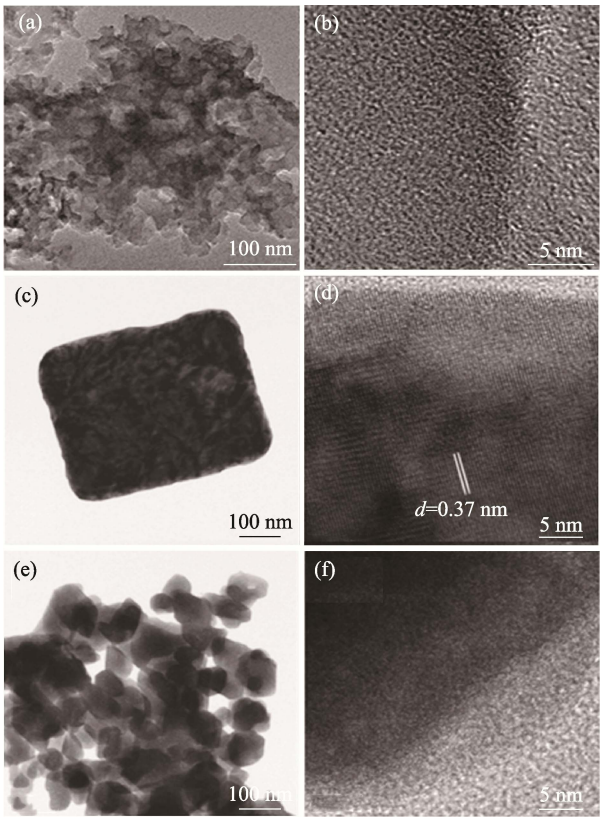

Fig. 2　TEM images of (a, b) HRP, (c, d) WO_3 and (e, f) 5%WO_3/HRP composite

(Fig. S3(a)). The high-resolution P2p spectrum of HRP (Fig. 3(a)) was deconvoluted into two peaks at 129.82 and 130.61 eV, corresponding to $P2p_{3/2}$ and $P2p_{1/2}$, respectively, and the binding energy peak at 134.19 eV corresponded to P–O bond, indicating the presence of phosphorus oxides on the surface of HRP. While in 5%WO_3/HRP composite, the P–O bond disappeared and the binding energies of the $P2p_{3/2}$ and $P2p_{1/2}$ were shifted towards higher binding energy, 130.12 and 130.97 eV, respectively, indicating that combination can prevent further oxidation of HRP. The W4f region of WO_3 (Fig. 3(b)) was divided into two peaks at 35.52 and 36.33 eV, assigned to $W4f_{5/2}$ and $W4f_{7/2}$ orbitals of W^{5+}. Another two peaks at 37.66 and 38.32 eV were corresponded to the $W4f_{5/2}$ and $W4f_{7/2}$ orbitals of W^{6+}. W^{5+} was derived from the unsaturated W–O bonds on the surface of WO_3. The presence of W^{5+} indicated the exfoliation of bulk WO_3 into ultrathin WO_3 nanosheets. The binding energy at 41.63 eV was associated with $W5f_{3/2}$[24]. While, the binding energies of $W4f_{5/2}$ and $W4f_{7/2}$ in the 5%WO_3/HRP composite shifted to low binding energy, and the ratio of W^{6+}/W^{5+} increased, which facilitated its energy conversion. Thus, when HRP was closely contacted with WO_3, the electrons could flow into WO_3 from HRP though the interface. Therefore, the heterojunction was formed between WO_3 and HRP, leading to strong electronic interaction.

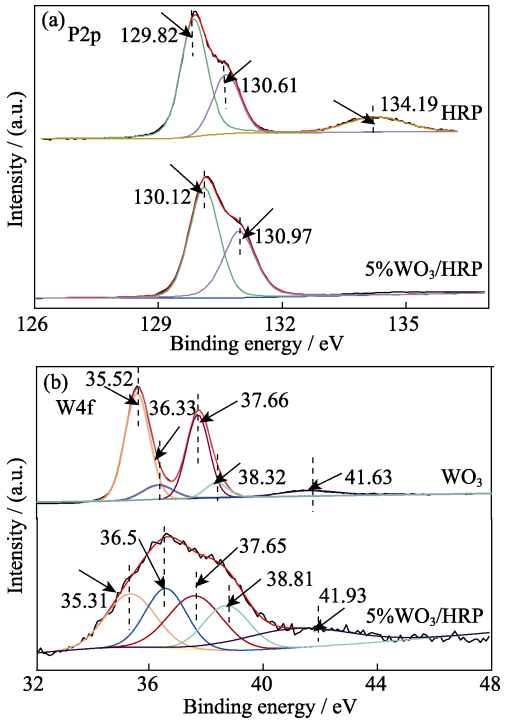

Fig. 3　(a) P2p and (b) W4f XPS spectra of samples

2.2　Photocatalytic performance

2.2.1　Photocatalytic degradation

The photodegradation performance of these catalysts was tested under visible light irradiation with RhB as the target pollutant (Fig. 4(a)). The equilibrium state of adsorption-desorption between the photocatalyst and the target pollutant was achieved after 30 min of reaction in the dark. Obviously, WO_3/HRP composites showed better adsorption capacity for RhB. Under visible light condition, the photodegradation performance of WO_3/HRP composites were higher than those of HRP and WO_3, and 5%WO_3/HRP composite was demonstrated the highest photocatalytic activity, and its removal rate reached 97.6% after 4 min. However, with further increasing of the WO_3/HRP ratio, the photocatalytic performance decreased since the excess WO_3 hinder the transfer of photogenerated carriers and reduce the exposure of active sites.

The photodegradation reactions of RhB in the synthesized samples conformed to the pseudo-first-order reaction model (Fig. 4(b)):

$$\ln(C_t/C_0') = -kt \quad (1)$$

where k is the rate consistent (min^{-1}), C_0' is the concentration of pollutants in the equilibrium of adsorption-desorption, and C_t is the concentration of contaminants for the remaining time after irradiation. The k of HRP, WO_3, 3%WO_3/HRP, 5%WO_3/HRP and 7%WO_3/HRP were 0.17, 0.01, 0.68, 0.75 and 0.69 min^{-1}, respectively. Among them, the k of 5%WO_3/HRP composite was highest, which was 4.5 and 75 times of those of HRP and WO_3. Therefore, the formation of heterojunction

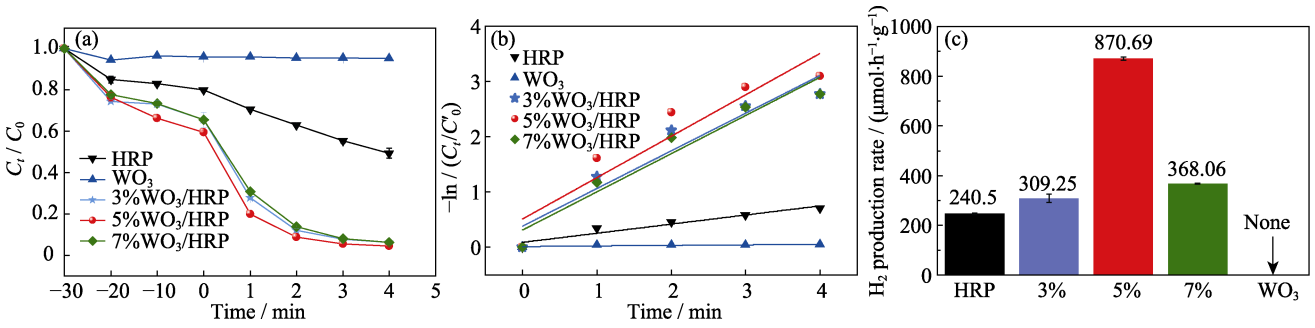

Fig. 4 (a) Photodegradation curves, (b) rate curves, and (c) hydrogen production rates of HRP, WO_3, 3%WO_3/HRP, 5%WO_3/HRP, and 7%WO_3/HRP composites

could enhance the photocatalytic activity. Furthermore, after five cycles of photocatalytic degradation of RhB, 5%WO_3/HRP composite still had high photocatalytic activity (90.4%), showing good stability with practical application potential.

2.2.2 Photocatalytic hydrogen evolution

The photoreduction ability of HRP, WO_3 and WO_3/HRP composites were examined by photocatalytic water splitting into hydrogen. HRP possessed a relatively low photocatalytic activity with hydrogen production rate of 240.5 μmol·h^{-1}·g^{-1}, and the pure WO_3 was almost absent, whereas a sharp increase in the rate of hydrogen production was observed in the WO_3/HRP composite (Fig. 4(c)). Fascinatingly, the hydrogen evolution rate of 5%WO_3/HRP composite was 870.69 μmol·h^{-1}·g^{-1}, which was 3.62 times of that of pure HRP. The apparent quantum efficiency (AQE) was calculated according to the following formula[26]:

$$\mathrm{AQE}= (2\cdot N_A\cdot M)/(E\lambda/(hc))\times 100\% \quad (2)$$

Where N_A is the Avogadro's constant (6.02×10^{23} mol^{-1}), M is the average H_2 generation rate (mol·s^{-1}), E is power of lamp source, h is the Plank's constant (6.626×10^{-34} J·s), λ is the excitation wavelength, and c is the speed of light (3.0×10^8 m·s^{-1}).

AQE of 5%WO_3/HRP composite was calculated to be 11.61%. Further increasing the amount of WO_3 beyond 5% lead to a decrease in photocatalytic hydrogen evolution rate, which could originate from shielding of the light absorption by excess amount of WO_3. Therefore, appropriate WO_3 content had a remarkable effect on the activity enhancement of WO_3/HRP composite.

The above RhB photodegradation and photocatalytic hydrogen evolution results exhibited that the 5%WO_3/HRP composite possessed superior photocatalytic activity. The introduction of appropriate WO_3 content inhibits the overgrowth and agglomeration of HRP, and the heterojunction between WO_3 and HRP promotes the separation of electrons and holes and accelerates the carrier migration.

2.3 Catalyst mechanism analysis

The optical absorption properties of prepared samples were investigated by UV-Vis DRS (Fig. 5(a)). HRP had significant absorption of visible light, meaning it was typical visible light photocatalytic material. For pure WO_3, the absorption edge was located at around 446 nm. Compared with pure WO_3 and HRP, the 5%WO_3/HRP composite had a red-shifted absorption edge, which illustrated enhancement of absorption in both UV and IR regions. The UV-visible light absorption performance of 5%WO_3/HRP composite combined the advantages of two materials, which successfully formed a heterojunction, and enhanced light-trapping ability. The band gap (E_g) values of the pure HRP and WO_3 were obtained through transformation with Kubella-Munk function, and were 1.9 and 2.78 eV, respectively (Fig. 5(b)).

The generation, migration, and recombination processes

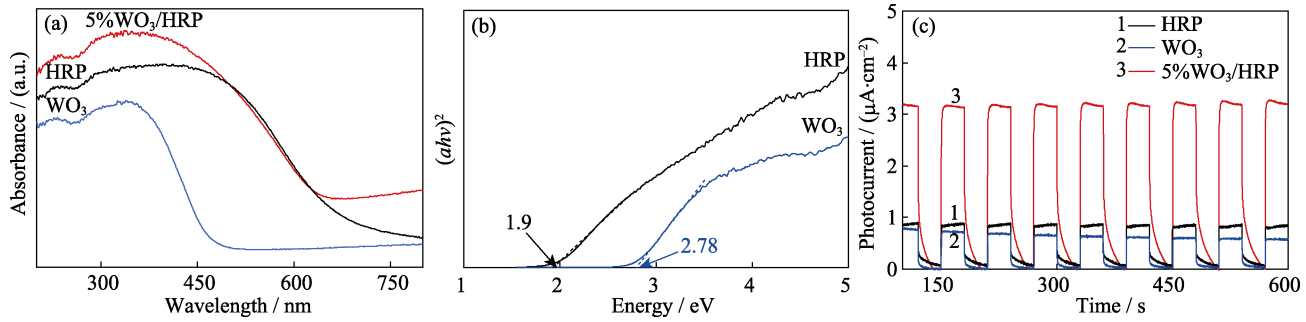

Fig. 5 (a) UV-Vis DRS spectra of HRP, WO_3 and 5%WO_3/HRP composite, (b) Tauc plots of HRP and WO_3, and (c) *I-t* curves of HRP, WO_3 and 5%WO_3/HRP composite

of photocarriers were investigated by PL spectra, transient photocurrent (*I-t*) curves and electrochemical impedance spectroscopy (EIS) measurements[29]. The 5%WO_3/HRP composite had lower PL signal, indicating lower recombination of photoinduced electrons and holes (Fig. S3(c)). In addition, the photocurrent signal intensity of the 5%WO_3/HRP composite was 3.3 μA/cm^2, which was 4~5 times of those of HRP (0.8 μA/cm^2) and WO_3 (0.7 μA/cm^2), respectively (Fig. 5(c)). These results implied that the lifetime of the photoexcited electron-hole pairs was significantly prolonged due to the more efficient separation, after combining HRP with WO_3.

The arc radius of 5%WO_3/HRP composite was smaller than those of HRP and WO_3, indicating the minimum charge impendence and the fastest reaction speed (Fig. 6(a)). This finding was consistent with the higher photocatalytic activity of the 5%WO_3/HRP composite due to the tight interface between WO_3 and HRP, which promoted carrier separation migration. Similarly, the equivalent circuit was analyzed to provide more intuitive understanding of the internal charge and surface charge-transfer mechanism of the catalyst during the reaction (insert in Fig. 6(a)). Here, R_1 and R_2 were denoted as the electrolyte solution and charge transfer resistances, which included the resistances of the photocatalyst, ITO substrate, electrolyte solution, and wire connections throughout the circuit. CPE_1 was the constant phase element that represents the bilayer capacitance of the charge transfer, and W_1 was the resistance with interfacial diffusion. R_1 of HRP, WO_3 and 5%WO_3/HRP were 10.1, 11.71 and 12.53 Ω, respectively. Under the same concentration, R_2 of HRP, WO_3, HRP and 5%WO_3/HRP were 672, 167 and 93.4 Ω, respectively. Obviously, the interfacial charge resistances of heterojunction composites were lower, indicating easier charge transfer. Therefore, the superior photocatalytic activity of 5%WO_3/HRP composite contributed to the highest photoelectric conversion efficiency, smaller interfacial transfer impendence and enhanced visible light absorption ability. The carrier lifetime (τ_e) of samples are based on the EIS bode plots (Fig. S4(a, b)), proving the carrier transfer process, according to the equation[30]:

$$\tau_e = 1/(2\pi f_{max}) \quad (3)$$

where f_{max} is the maximum frequency peak position, the calculated τ_e of the HRP and 5%WO_3/HRP composite were 1.68 and 2.7 ms, respectively. The carrier lifetime of 5%WO_3/HRP heterostructure composite was much longer than those of pure HRP, suggesting that the formation of the heterostructure between HRP and WO_3 could greatly prolong the lifetime of the photo-generated electrons, and enhanced the photocatalytic activity.

2.4 Photogenerated carrier analysis

The energy band structures of samples were revealed by Mott-Schott (M-S) measurements (Fig. 6(b)). The flat potentials (E_{fb}) of HRP and WO_3 were –0.8 and –0.66 V (*vs*. Ag/AgCl), respectively, and then converted to the hydrogen standard electrode potential based on the formula:

$$E_{fb}\ (vs.\ \text{NHE}) = E_{fb}\ (\text{pH } 0,\ vs.\ \text{Ag/AgCl}) + E_{AgCl} + 0.059 \cdot \text{pH} \quad (4)$$

Where E_{AgCl} is 0.197 V, and pH of the electrolyte was 6.8. Here, E_{fb} (*vs*. NHE) of HRP and WO_3 were –0.2 and –0.06 V, respectively. The slopes of WO_3 and HRP curves were positive, both samples were n-type semiconductors, and E_{fb} is 0.1–0.3 V higher than its conduction band potential (E_{CB}). Therefore, the E_{CB} of HRP and WO_3 were –0.4 and –0.26 V (*vs*. NHE). In accordance with the formula: $E_g = E_{VB} - E_{CB}$, the E_{VB} were 1.5 and 2.52 V, respectively.

The hydroxyl radicals (·OH) was important species in the photocatalytic reactions, EPR spectra were presented in Fig. 6(c). HRP had relatively weak signal because of the weak oxidation potential of photogenerated holes, WO_3 displayed moderately strong signal due to its more positive E_{VB}, and 5%WO_3/HRP composite had strong DMPO-·OH signal, so the photogenerated holes remained in WO_3 and did not transfer to the VB of HRP. Because the potential of OH^-/·OH pair was +2.38 V (*vs*. NHE)[31], which was positive than that of HRP (+1.5 V (*vs*. NHE)) and negative than that of the WO_3 (+2.52 V

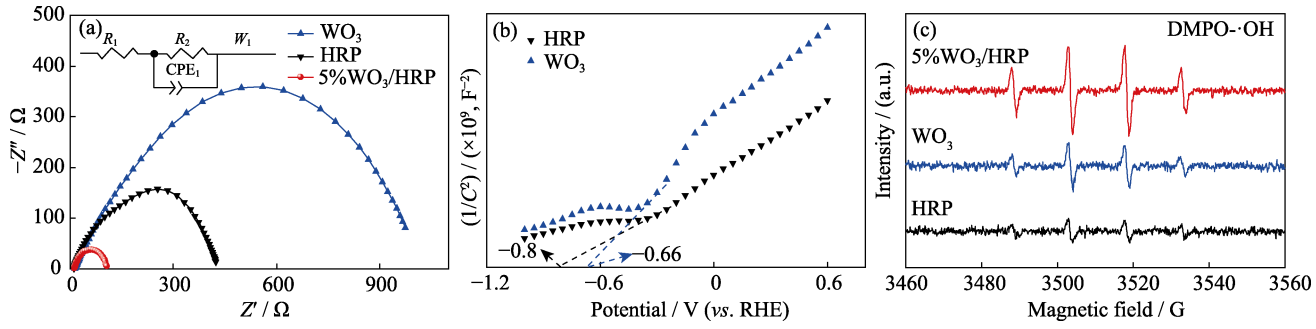

Fig. 6　(a) EIS spectra of HRP, WO_3 and 5%WO_3/HRP composite, (b) Mott-Schottky curves of HRP and WO_3, and (c) EPR spectra of HRP, WO_3 and 5%WO_3/HRP composite

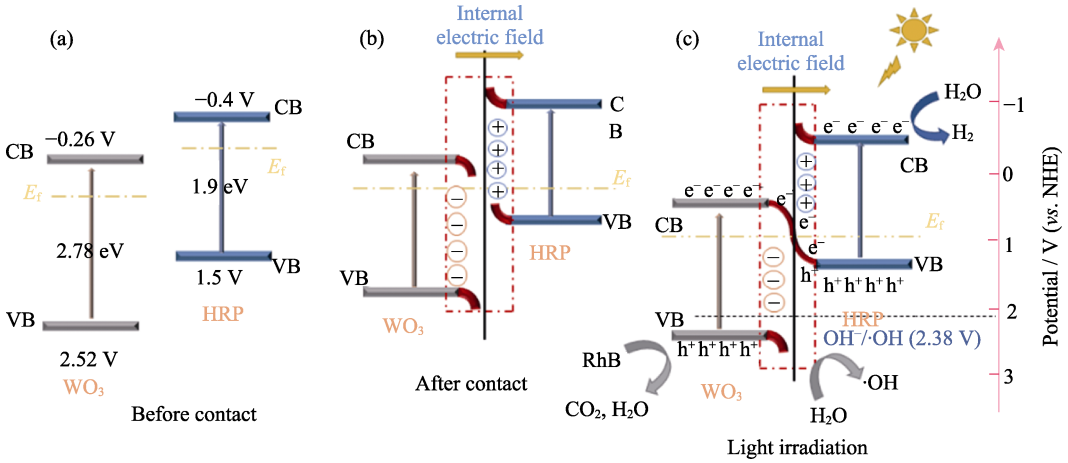

Fig. 7 Photocatalytic mechanism of the WO_3/HRP composite

(a) Before contact; (b) After contact in darkness; (c) S-scheme transfer process of photogenerated carriers under visible light irradiation

(*vs.* NHE), inferring that the ·OH radical was produced by WO_3. These results indicated that the photogenerated electrons and holes in 5%WO_3/HRP composite were present in the CB of HRP and VB of WO_3, respectively, and the charge transfer belonged to S-scheme heterojunction.

Based on above discussions, the S-scheme mechanism was proposed in Fig. 7. HRP is a reducing photocatalyst with smaller work function (5.61 eV)[17] and higher Fermi level. WO_3 is an oxidizing photocatalyst with large work function (6.23 eV)[32] and lower Fermi level (Fig. 7(a)). When the WO_3 photocatalysts was in close contact with HRP, electrons spontaneously transferred from HRP to WO_3 until their E_f reached the same level. During the migration of electrons, the interface region of WO_3 possesses a positive charge due to the loss of electrons, which leads to the formation of electron depletion layer and the upward bending of the energy band. While interface region near the HRP is negatively charged due to the gain of electrons, which leads to the formation of an electron accumulation layer and the downward bending of the band edge. As a result, an internal electric field is formed at the interface of the WO_3/HRP heterojunction, impeding the continuous flow of electrons from HRP to WO_3 (Fig. 7(b)). Under visible light irradiation, the electrons were excited from VB to CB of WO_3 and HRP. Driven by the internal electric field, band bending and Coulomb interaction, the photogenerated electrons in the CB of WO_3 spontaneously slid toward HRP, and recombined with the holes on the VB of HRP. However, the useful electrons and holes of strong redox ability could be retained (Fig. 7(c)). Therefore, the improved photocatalytic performance of the WO_3/HRP composite was mainly ascribed to the formation of S-scheme heterojunctions, which contribute to the strong redox capacity for the degradation of organic water pollutants and hydrogen generation.

3 Conclusions

In this study, the S-scheme WO_3/HRP heterojunction photocatalysts were prepared by the hydrothermal method. The heterojunctions displayed significantly enhanced photocatalytic RhB degradation and hydrogen evolution. The 5%WO_3/HRP heterojunction photocatalysts degraded 97.6% RhB within 4 min. Meanwhile, the photocatalytic hydrogen evolution was almost 3.62 times of pure HRP. The enhanced photocatalytic performance was attributed to the S-scheme heterojunction between WO_3 and HRP, which effectively transferred the photo- generated carriers, and suppressed the recombination of electron-hole pairs. This work could provide new prospect for design and construction of novel heterojunction photocatalyst.

References:

[1] TAO J, ZHANG M, GAO X, *et al.* Photocatalyst Co_3O_4/red phosphorus for efficient degradation of malachite green under visible light irradiation. *Materials Chemistry and Physics*, 2020, **240:** 122185.
[2] LIU E, QI L, CHEN J, *et al. In situ* fabrication of a 2D Ni_2P/red phosphorus heterojunction for efficient photocatalytic H_2 evolution. *Materials Research Bulletin*, 2019, **115:** 27.
[3] LIANG Z, DONG X, HAN Y, *et al. In-situ* growth of 0D/2D Ni2P quantum dots/red phosphorus nanosheets with p-n heterojunction for efficient photocatalytic H_2 evolution under visible light. *Applied Surface Science*, 2019, **484:** 293.
[4] WU C, JING L, DENG J, *et al.* Elemental red phosphorus-based photocatalysts for environmental remediation: a review. *Chemosphere*, 2021, **274:** 129793.
[5] WANG Z, BAI Y, LI Y, *et al.* $Bi_2O_2CO_3$/red phosphorus S-scheme heterojunction for H_2 evolution and Cr(VI) reduction. *Journal of Colloid and Interface Science*, 2022, **609:** 320.
[6] ZHU Y, LI J, DONG C, *et al.* Red phosphorus decorated and doped TiO_2 nanofibers for efficient photocatalytic hydrogen evolution from pure water. *Applied Catalysis B: Environmental*, 2019, **255:** 117764.
[7] AIHEMAITI X, WANG X, LI Y, *et al.* Enhanced photocatalytic and antibacterial activities of S-scheme SnO_2/Red phosphorus photocatalyst under visible light. *Chemosphere*, 2022, **296:** 134013.
[8] ZHU E, MA Y, DU H, *et al.* Three-dimensional bismuth oxide/red phosphorus heterojunction composite with enhanced photoredu-

ction activity. *Applied Surface Science*, 2020, **528:** 146932.
[9] WANG Z, BAI Y, LI Y, *et al.* $Bi_2O_2CO_3$/red phosphorus S-scheme heterojunction for H_2 evolution and Cr(VI) reduction. *Journal of Colloid and Interface Science*, 2022, **609:** 320.
[10] WANG W, LI G, AN T, *et al.* Photocatalytic hydrogen evolution and bacterial inactivation utilizing sonochemical-synthesized g-C_3N_4/red phosphorus hybrid nanosheets as a wide-spectral-responsive photocatalyst: the role of type I band alignment. *Applied Catalysis B: Environmental*, 2018, **238:** 126.
[11] ZHU E, ZHAO S, DU H, *et al.* Construction of $Bi_2Fe_4O_9$/red phosphorus heterojunction for rapid and efficient photo-reduction of Cr(VI). *Journal of the American Ceramic Society*, 2021, **104:** 5411.
[12] ZHOU L, LI Y, YANG S, *et al.* Preparation of novel 0D/2D Ag_2WO_4/WO_3 step-scheme heterojunction with effective interfacial charges transfer for photocatalytic contaminants degradation and mechanism insight. *Chemical Engineering Journal*, 2021, **420:** 130361.
[13] ZHANG J, LIU Z, LIU Z. Novel WO_3/Sb_2S_3 heterojunction photocatalyst based on WO_3 of different morphologies for enhanced efficiency in photoelectrochemical water splitting. *ACS Applied Materials & Interfaces*, 2016, **8(15):** 9684.
[14] LING Y, DAI Y. Direct Z-scheme hierarchical WO_3/BiOBr with enhanced photocatalytic degradation performance under visible light. *Applied Surface Science*, 2020, **509:** 145201.
[15] SONG C, WANG X, ZHANG J, *et al.* Enhanced performance of direct Z-scheme CuS-WO_3 system towards photocatalytic decomposition of organic pollutants under visible light. *Applied Surface Science*, 2017, **425:** 788.
[16] JIANG S, CAO J, GUO M, *et al.* Novel S-scheme WO_3/RP composite with outstanding overall water splitting activity for H_2 and O_2 evolution under visible light. *Applied Surface Science*, 2021, **558:** 149882.
[17] TUERHONG M, CHEN P, MA Y, *et al.* Bi_2MoO_6/red phosphorus heterojunction for reducing Cr(VI) and mitigating *Escherichia coli* infection. *Journal of Solid State Chemistry*, 2022, **315:** 123468.
[18] PAN T, CHEN D, XU W, *et al.* Anionic polyacrylamide-assisted construction of thin 2D-2D WO_3/g-C_3N_4 step-scheme heterojunction for enhanced tetracycline degradation under visible light irradiation. *Journal of Hazardous Materials*, 2020, **393:** 122366.
[19] ZHANG N, LI X, YE H, *et al.* Oxide defect engineering enables to couple solar energy into oxygen activation. *Journal of the American Chemical Society*, 2016, **138(28):** 8928.
[20] XIAO T, TANG Z, YANG Y, *et al. In situ* construction of hierarchical WO_3/g-C_3N_4 composite hollow microspheres as a Z-scheme photocatalyst for the degradation of antibiotics. *Applied Catalysis B: Environmental*, 2018, **220:** 417.
[21] GUO C, DU H, MA Y, *et al.* Visible-light photocatalytic activity enhancement of red phosphorus dispersed on the exfoliated kaolin for pollutant degradation and hydrogen evolution. *Journal of Colloid and Interface Science*, 2020, **585**: 167.
[22] ZHOU J, AN X, TANG Q, *et al.* Dual channel construction of WO_3 photocatalysts by solution plasma for the persulfate-enhanced photodegradation of bisphenol A. *Applied Catalysis B: Environmental*, 2020, **277:** 119221.
[23] FENG C, TANG L, DENG Y, *et al.* Synthesis of branched WO_3@$W_{18}O_{49}$ homojunction with enhanced interfacial charge separation and full-spectrum photocatalytic performance. *Chemical Engineering Journal*, 2020, **389:** 124474.
[24] ZHANG K, JIN B, PARK C, *et al.* Black phosphorene as a hole extraction layer boosting solar water splitting of oxygen evolution catalysts. *Nature Communications*, 2019, **10(1):** 2001.
[25] ZOU X, DONG Y, KE J, *et al.* Cobalt monoxide/tungsten trioxide p-n heterojunction boosting charge separation for efficient visible-light-driven gaseous toluene degradation. *Chemical Engineering Journal*, 2020, **400:** 125919.
[26] YUE X, YI S, WANG R, *et al.* Well-controlled $SrTiO_3$@Mo_2C core-shell nanofiber photocatalyst: boosted photo-generated charge carriers transportation and enhanced catalytic performance for water reduction. *Nano Energy*, 2018, **47:** 463.
[27] AIHEMAITI X, WANG X, WANG Z, *et al.* Effective prevention of charge trapping in red phosphorus with nanosized CdS modification for superior photocatalysis. *Journal of Environmental Chemical Engineering*, 2021, **9(6):** 106479.
[28] DONG C, YANG Y, HU X, *et al.* Self-cycled photo-Fenton-like system based on an artificial leaf with a solar-to-H_2O_2 conversion efficiency of 1.46%. *Nature Communications*, 2022, **13(1):** 4982.
[29] GE H, XU F, CHENG B, *et al.* S-scheme heterojunction TiO_2/CdS nanocomposite nanofiber as H_2-production photocatalyst. *ChemCatChem*, 2019, **11(24):** 6301.
[30] LIU Y, PAN D, XIONG M, *et al. In-situ* fabrication SnO_2/SnS_2 heterostructure for boosting the photocatalytic degradation of pollutants. *Chinese Journal of Catalysis*, 2020, **41(10):** 1554.
[31] JIA Y, WANG Z, QIAO X, *et al.* A synergistic effect between S-scheme heterojunction and Noble-metal free cocatalyst to promote the hydrogen evolution of ZnO/CdS/MoS_2 photocatalyst. *Chemical Engineering Journal*, 2021, **424:** 130368.
[32] FU J, XU Q, LOW J, *et al.* Ultrathin 2D/2D WO_3/g-C_3N_4 step-scheme H_2-production photocatalyst. *Applied Catalysis B: Environmental*, 2019, **243:** 556.

单晶 WO_3/红磷 S 型异质结的构建及光催化活性研究

吐尔洪·木尼热[1], 赵红刚[1,2], 马玉花[1,2], 齐献慧[1],
李钰宸[1], 闫沉香[1], 李佳文[1], 陈　平[1]

(新疆师范大学 1. 化学化工学院; 2.新疆储能与光电催化材料重点实验室, 乌鲁木齐 830054)

摘　要: S 型异质结被广泛应用于光解水产氢和解决环境污染问题。本研究通过简单的水热法制备了单晶 WO_3/水热处理后的红磷(HRP)复合材料。XPS 和 EPR 等表征结果证实单晶 WO_3/HRP 复合材料形成了 S 型异质结。5%WO_3/HRP 异质结复合物在可见光下展现出最佳的光催化活性, 在 4 min 内对罗丹明 B(RhB)的降解率高达 97.6%。此外, 制氢速率可以达到 870.69 μmol·h^{-1}·g^{-1}, 是纯 HRP 的 3.62 倍。这可归功于单晶 WO_3 和 HRP 之间形成紧密的 S 型异质结, 使其光生载流子快速分离并提高氧化还原能力。本研究制备的 RP 基光催化剂为解决日益增长的清洁新能源和饮用水需求提供了参考。

关　键　词: WO_3; 红磷; 光解水产氢; S 型异质结

中图分类号: O643　　**文献标志码:** A

Supplementary Material :

Construction and Photocatalytic Activity of Monoclinic Tungsten Oxide/Red Phosphorus Step-scheme Heterojunction

TUERHONG Munire[1], ZHAO Honggang[1,2], MA Yuhua[1,2], QI Xianhui[1], LI Yuchen[1], YAN Chenxiang[1], LI Jiawen[1], CHEN Ping[1]

(1. College of Chemistry and Chemical Engineering, Xinjiang Normal University, Urumqi 830054, China; 2. Xinjiang Key Laboratory of Energy Storage and Photoelectrocatalytic Materials, Xinjiang Normal University, Urumqi 830054, China)

1 Experimental

1 Characterization

The crystal structures of the catalysts were determined by X-ray diffractometer (XRD, D8 Advance) with Cu-Kα radiation (λ=0.154178 nm) in the range of 2θ=10°–80°. The functional groups of the samples were characterized by using Fourier transform infrared spectroscopy (FT-IR, TENSOR27). The morphologies of the as-synthesized samples were observed by field emission scanning electron microscope (FESEM, Zeiss Sigma 500). The phase structures of samples were examined with the high-resolution transmission electron microscope (HRTEM, FEI Tecnai F20). The surface chemical elements and the valence states of catalysts were characterized by using X-ray photoelectron spectroscopy (XPS, ESCALAB 250Xi). The optical absorption of the samples was analyzed by ultraviolet-visible spectrometer (UV-Vis DRS, PE lambda 750S). The photoluminescence spectrum of the sample was measured by Transient fluorescence spectrometer (PL, Edinburgh FLS9800). In addition, all electrochemical experiments were carried out by using three electrodes electrochemical workstation (CHI660D), the counter electrode, reference electrode and electrolyte in the electrochemical characterization were Pt electrode, Ag/AgCl electrode, and 0.1 mol/L Na_2SO_4 solution, respectively.

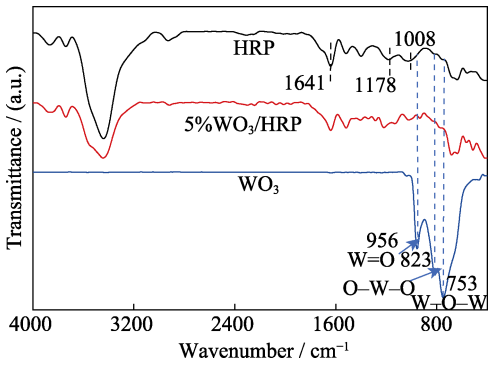

Fig. S1 FT-IR spectra of HRP, WO_3 and 5%WO_3/HRP composite

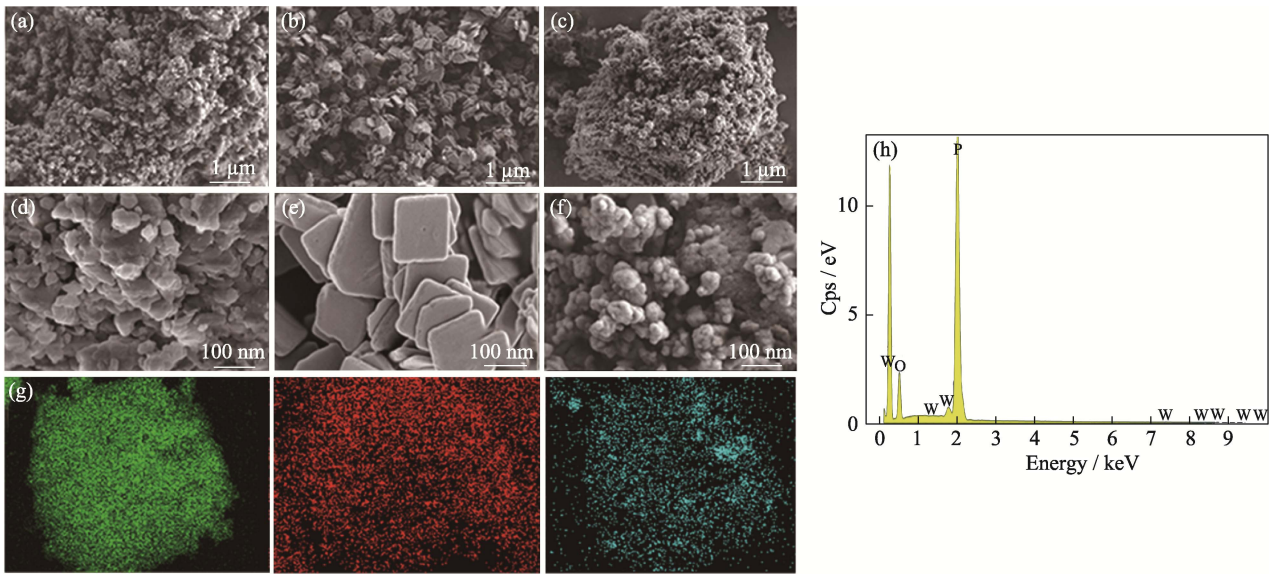

Fig. S2 SEM images of (a, d) HRP, (b, e) WO_3, (c, f) 5%WO_3/HRP composite, and (g) corresponding elemental mapping of P, O and W, and (h) EDS spectra of 5%WO_3/HRP composite

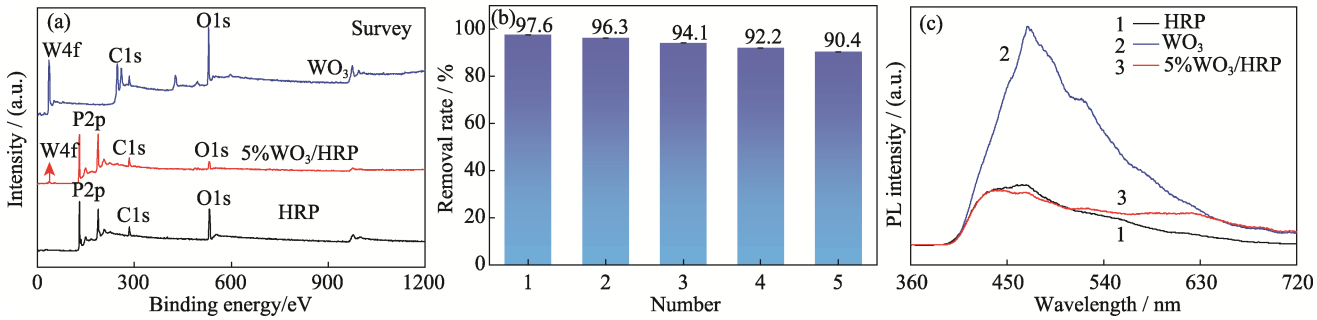

Fig. S3　(a) XPS survey spectra of HRP, WO_3, 5%WO_3/HRP composite, (b) cycling performance of RhB photodegradation by 5%WO_3/HRP composite and (c) PL spectra of HRP, WO_3, 5%WO_3/HRP composite

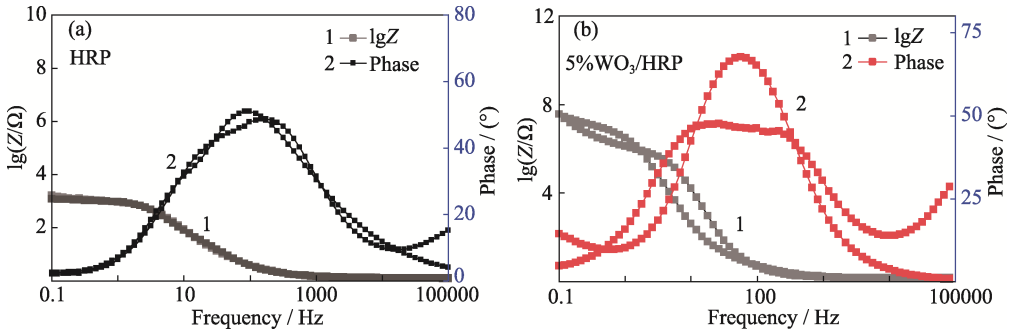

Fig. S4　EIS Bode plots of (a) HRP and (b) 5%WO_3/HRP composite